International Journal of Biological Macromolecules 229 (2023) 224–235

Contents lists available at ScienceDirect

International Journal of Biological Macromolecules

journal homepage: www.elsevier.com/locate/ijbiomac

Reduced graphene oxide-enriched chitosan hydrogel/cellulose acetate-based nanofibers application in mild hyperthermia and skin regeneration

Mariana F.P. Graça [a], Bruna L. Melo [a], Rita Lima-Sousa [a], Paula Ferreira [b,c], André F. Moreira [a,d,*], Ilídio J. Correia [a,b,*]

[a] CICS-UBI – Centro de Investigação em Ciências da Saúde, Universidade da Beira Interior, Av. Infante D. Henrique, 6200-506 Covilhã, Portugal
[b] CIEPQPF – Departamento de Engenharia Química, Universidade de Coimbra, Rua Silvio Lima, 3030-790 Coimbra, Portugal
[c] Instituto Superior de Engenharia de Coimbra, Instituto Politécnico de Coimbra, Rua Pedro Nunes, 3030-199 Coimbra, Portugal
[d] CPIRN-UDI/IPG – Center of Potential and Innovation in Natural Resources, Research Unit for Inland Development, Instituto Politécnico da Guarda, Avenida Dr. Francisco de Sá Carneiro, 6300-559 Guarda, Portugal

ARTICLE INFO

Keywords:
Asymmetric wound dressings
Near-infrared radiation
Skin regeneration

ABSTRACT

Asymmetric wound dressings have captured researchers' attention due to their ability to reproduce the structural and functional properties of the skin layers. Furthermore, recent studies also report the benefits of using near-infrared (NIR) radiation-activated photothermal therapies in treating infections and chronic wounds. Herein, a chitosan (CS) and reduced graphene oxide (rGO) hydrogel (CS_rGO) was combined with a polycaprolactone (PCL) and cellulose acetate (CA) electrospun membrane (PCL_CA) to create a new NIR-responsive asymmetric wound dressing. The rGO incorporation in the hydrogel increased the NIR absorption capacity and allowed a mild hyperthermy effect, a temperature increase of 12.4 °C when irradiated with a NIR laser. Moreover, the PCL_CA membrane presented a low porosity and hydrophobic nature, whereas the CS_rGO hydrogel showed the ability to provide a moist environment, prevent exudate accumulation and allow gaseous exchanges. Furthermore, the *in vitro* data demonstrate the capacity of the asymmetric structure to act as a barrier against bacteria penetration as well as mediating a NIR-triggered antibacterial effect. Additionally, human fibroblasts were able to adhere and proliferate in the CS_rGO hydrogel, even under NIR laser irradiation, presenting cellular viabilities superior to 90 %. Altogether, our data support the application of the NIR-responsive asymmetric wound dressings for skin regeneration.

1. Introduction

Skin is the outer barrier of the human body and it is responsible for providing protection against external factors (*e.g.*, microorganisms), assisting in sensory functions, maintaining homeostasis, and controlling the body temperature [1]. During an individuals' lifetime, the skin will be subjected to different events, such as diseases or injuries, that can compromise its normal structure and function. To surpass such health conditions, wound dressings arise as promising and efficient solutions for supporting and accelerating the wound healing process, particularly when the natural ability of the skin to self-heal is not enough to reestablish this ultimate barrier of the body [1]. Nevertheless, traditional wound dressings (*e.g.*, gauzes, bandages, creams, and artificial skin grafts) still fail to fully re-establish the structure and functions of the native skin [2].

Nowadays, asymmetric wound dressings have been widely explored for biomimetic purposes, *i.e.* to reproduce the layered structure of the skin. Specifically, these dressings usually present a hydrophobic top layer that acts as a protective barrier (similar to the epidermis) and a hydrophilic bottom layer that maintains a moist environment as well as promotes cell adhesion and proliferation (resembling the dermis) [2–4]. Moreover, asymmetric wound dressings combine the advantages observed in the simpler alternatives (*i.e.*, membranes, hydrogels, sponges, and nanofibers), creating a more effective wound dressing. Dense electrospun membranes with small pore sizes have been explored as the top layer due to its ability to act as an occlusive barrier, mainly

* Corresponding author.
E-mail addresses: afmoreira@fcsaude.ubi.pt (A.F. Moreira), icorreia@ubi.pt (I.J. Correia).

https://doi.org/10.1016/j.ijbiomac.2022.12.291
Received 24 October 2022; Received in revised form 19 December 2022; Accepted 25 December 2022
Available online 29 December 2022

avoiding the colonization of the wound site by microorganisms, while still allowing gaseous exchanges and presenting good mechanical properties [2]. On the other hand, several studies have also been focused on producing hydrogels for the bottom layer with natural polymers (*e.g.*, silk fibroin, chitosan (CS), and lignin), antibacterial agents, or even combining these different approaches in one system using green protocols [5–13]. This bottom layer is conceived to support skin regeneration, mediating processes such as cell adhesion and avoiding exudate accumulation [2]. For example, Miguel et al. developed a 3D asymmetric skin construct composed of an electrospun membrane (top layer) and a 3D bioprinted hydrogel (bottom layer). The denser top layer of the dressing was designed to protect the wound site, while the porous bottom layer was able to absorb the excess of exudate as well as support cell migration, adhesion, and proliferation [2].

Despite the closer structural resemblance displayed by asymmetric wound dressings in comparison with the skin, researchers are still facing important challenges, namely in the treatment of chronic wound infections. In this area, the search for alternatives to conventionally used antibiotics, due to the development of multi-drug resistance mechanisms by bacteria, has been one of the main objectives [13]. Several works have been pointing to the efficacy of light-responsive agents (*e.g.*, near-infrared (NIR) radiation) in preventing or treating established infections, either by generating heat (photothermal therapy) or reactive oxygen species (photodynamic therapy) [14–16]. Moreover, the optimization of the heat generation to induce mild hyperthermia (*i.e.*, a local increase of the temperature to $\leq$48 °C) can also enhance the wound-healing process [17–20]. For that purpose, different NIR-responsive nanomaterials, such as indocyanine green, polydopamine, copper sulfide, and graphene oxide (GO), have been incorporated in the wound dressings. Among them, GO has been demonstrating an excellent capacity to convert NIR light into heat and to improve the mechanical properties of biomaterials [21]. Zhang et al. produced carboxymethylated CS/aldehyde terminated polyethylene glycol hydrogel enriched with branched polyethyleneimine modified with graphene oxide to be applied in mild photothermal therapy and wound management [22]. After NIR irradiation (808 nm, for 5 min), the hydrogels reached a maximum temperature of 33.0 °C, 38.6 °C, 41.5 °C, and 45.9 °C by increasing the irradiation intensity from 1.0 W/cm^2, 1.5 W/cm^2, 2.0 W/cm^2, to 2.5 W/cm^2. Furthermore, the wounds treated with NIR + hydrogel were completely closed after 14 days, while the relative wound areas in the control, NIR, and hydrogel groups were 21.6 %, 20.7 %, and 14.1 %, respectively [22]. Reduced GO (rGO), a derivative of GO, has also been used due to its higher absorbance of NIR light as well as antibacterial and pro-angiogenic properties [21,23,24]. Zárate et al. developed electrospun meshes (with random or aligned fibers) containing 0.5 or 1 % of rGO and analyzed its photothermal capacity in different conditions and under NIR light [25]. The electrospun meshes with random fibers could achieve a final temperature of 37.8 °C with 0.5 % of rGO and 52.3 °C with 1 % of rGO. For the electrospun meshes with aligned fibers, the registered final temperatures reached 33 °C and 49.3 °C, with 0.5 % or 1 % of rGO, respectively [25]. Therefore, the rGO NIR-triggered mild photothermal effect can be a promising and straightforward approach for increasing the bioactivity of asymmetric wound dressings.

Herein, a NIR-responsive asymmetric wound dressing (AWD) was developed to prevent the occurrence of skin infections and to improve the wound healing process. The asymmetric system was composed of a top layer based on a polycaprolactone (PCL) and cellulose acetate (CA) electrospun membrane (PCL_CA) and a CS_rGO hydrogel (CS_rGO) as the bottom layer. This structural organization aimed to create a dense top layer that provides hydrophobicity and protection to the wound site, and a porous hydrophilic bottom layer that promotes exudate absorption and cell migration, adhesion, and proliferation. Furthermore, the rGO NIR-responsive photothermal agent will be explored to mediate a mild hyperthermy effect, for enhancing the antibacterial properties and the wound healing process.

2. Materials and methods

2.1. Materials

Dopamine hydrochloride (MW = 189.64 g/mol) and Trifluoroethanol (TFE) were obtained from Acros Organics (China). Fetal bovine serum (FBS) free from antibiotics was bought from Biochrom AG (Berlin, Germany). $NaHCO_3$ was acquired from Fisher Scientific (Oeiras, Portugal). Cell culture plates and T-flasks were purchased from Thermo Fisher Scientific (Porto, Portugal). Normal human dermal fibroblasts (NHDF) cells were acquired from PromoCell (Labclinics, S.A., Barcelona, Spain). 3-(4,5-dimethylthiazol-2-yl)-5-(3-carboxymethoxyphenyl)-2 (4-sulfophenyl)-2H-tetrazolium (MTS) was obtained from Promega (Madison, WI, USA). CS with low molecular weight (50,000–190,000 Da; deacetylation degree $\geq$75 %), Dulbecco's modified eagle's medium F-12 (DMEM-F12), CA (MW = 30,000 Da), PCL (MW = 70,000–90,000 Da), Resazurin, Glutaraldehyde, GO (it was sonicated for 6 h before being used), LB Broth, Phosphate buffered saline solution (PBS), Triton X-100 and trypsin were purchased from Sigma-Aldrich (Sintra, Portugal). Propidium Iodide (PI) buffer was acquired from Life Technologies (Maryland, USA). Tris Base was supplied by ThermoFisher Scientific (Waltham, MA, USA). *Staphylococcus aureus* (*S. aureus*) ATCC 25923 clinical isolate and *Escherichia coli DH5α* (*E. coli*) were used to evaluate the antimicrobial properties of the wound dressings. Double deionized and filtered water (0.22 μm filtered; 18.2 MΩ/cm at 25 °C) was obtained using a Milli-Q Advantage A10 ultrapure Water Purification System.

2.2. Methods

2.2.1. Production of the electrospun membrane

The production of the electrospun membrane was performed by using a conventional electrospinning apparatus, composed of a high-voltage source (Spellman SL40*10,

0–40 kV; acquired to Spellman, Corporate Headquarters USA), a precision syringe pump (KDS-100), a plastic syringe with a stainless-steel needle (21 Gauge), and a collector. The electrospun membrane (PCL_CA) was produced with a polymeric mixture of PCL (10 % *w/v*) with CA (7 % w/v) dissolved in TFE (80 % *v*/v). To accomplish that, the solution was loaded in the syringe and electrospun at a constant flow rate of 1.2 mL/h, applied voltage of 20 kV, and collector distance of 15 cm.

2.2.2. Production and characterization of the hydrogels

The CS-based hydrogels incorporating different concentrations of rGO (CS_rGO100–100 μg/mL and CS_rGO200–200 μg/mL of rGO) were assembled following a protocol previously described [26]. Initially, the gelling agent was prepared through the dissolution of $NaHCO_3$ in PBS. Afterward, 200 μL of gelling agent's solution were mixed with 600 μL of CS (2.75 % (*w/v*)) and 400 μL of rGO. Then, 400 μL of the gelling agent/CS/rGO mixture was pipetted into hollow cylindrical templates (ϕ = 8 mm; height = 4 mm) for attaining the CS_rGO hydrogels.

The gelation capacity of the different CS_rGO hydrogels was confirmed by the tube inversion test [27]. In addition, rheological studies (constant speed of 60 rpm, 15 s intervals, at room temperature (RT)) were also carried out in a Thermostated Brookfield DV3T cone-plate rheometer using a CP52Z cone (Brookfield Ametek, Massachusetts, USA) to characterize the CS_rGO hydrogels' viscosity at different time points [27]. Results were disregarded if the torque value was superior to 95 % and inferior to 5 %. Furthermore, the mechanical properties strain, compressive strength (Cstrength) and young's modulus (YM)) of the produced hydrogels were characterized using a TA.XTplus Texture Analyzer and calculated using the following equations:

$$\text{Strain}\ (\%) = \frac{\Delta l}{l} \quad (1)$$

$$\text{Compressive strength (kPa)} = \frac{F}{A} \quad (2)$$

$$\text{Young's modulus (kPa)} = \frac{\text{Compressive strength}}{\text{Strain}} \quad (3)$$

where Δl is the change in length; l is the total length; F is the applied force; and A is the superficial area.

The AWD was assembled by depositing the CS_rGO100 or CS_rGO200 hydrogel on the top of PCL_CA electrospun membranes, originating the AWD_100 and AWD_200 samples, respectively.

2.2.3. Characterization of the photothermal capacity of the hydrogels

The optical absorption properties of CS_rGO solutions were characterized using an Evolution 201 UV–vis-NIR spectrophotometer (Thermo Scientific Inc., Massachusetts, USA). Moreover, the photothermal capacity of CS_rGO100 and CS_rGO200 was determined by monitoring the temperature changes in response to the NIR laser irradiation [26]. Briefly, the hydrogels were immersed in water, exposed to NIR irradiation for 10 min (808 nm, 1.7 W/cm^2), and the temperature changes were registered at predetermined timepoints by using a thermocouple thermometer. Double deionized and filtered water exposed to the NIR light was used as control.

2.2.4. Characterization of the layers' morphology and chemical properties

Scanning electron microscopy (SEM) was used to characterize the surface morphology and porosity of the produced membranes, hydrogels, and AWD [2]. To accomplish that, samples were mounted onto aluminum stubs using Araldite glue and coated with gold using a Quorum Q150R ES sputter coater (Quorum Technologies Ltd., Laughton, East Sussex, UK). Then, SEM images were obtained using a Hitachi S-3400 N Scanning Electron Microscope (Hitachi, Tokyo, Japan) operated at an accelerating voltage of 20 kV. Moreover, the PCL_CA nanofibers' average diameter was determined by using ImageJ software (Scion Corp., Frederick, MD).

In addition, attenuated total reflectance-Fourier transform infrared (ATR_FTIR) spectroscopy was used to evaluate the chemical composition of the electrospun membrane and hydrogels. The materials' spectra were acquired in a Nicolet iS10 FTIR spectrophotometer (Thermo Scientific, Waltham, MA, USA) using an average of 128 scans, spectral width of 4000 to 400 cm^{-1}, and spectral resolution of 4 cm^{-1}.

2.2.5. Determination of the porosity

The total porosity of the produced membranes was determined by using the liquid displacement method [28]. For that purpose, the samples ($n = 5$) were weighted, immersed in absolute EtOH for 1 h, and reweighted. Subsequently, the membranes' porosity was determined through Eq. (4):

$$\text{Porosity (\%)} = \frac{W_w - W_d}{D_{ethanol} * V_{membrane}} \times 100 \quad (4)$$

where W_w and W_d are the wet and dry weights of the membrane, respectively. $D_{ethanol}$ represents the density of EtOH at RT, and $V_{membrane}$ is the volume of the wet membrane.

2.2.6. Evaluation of the swelling profile

The swelling capacity of the samples was determined after incubation under stirring (60 rpm) in Tris-HCL solution (pH 5 and pH 8) at 37 °C [29]. Then, at specific time points, the Tris-HCL was removed and the samples ($n = 5$) were weighted. Finally, the swelling ratio was calculated through Eq. (5):

$$\text{Swelling ratio} = \frac{W_t}{W_0} \quad (5)$$

where W_t is the weight of the samples at time t and W_0 is the initial weight of the samples.

Furthermore, hydrogel samples were also collected after 7 days of incubation in Tris-HCL solution (pH 5 and pH 8) and analyzed by SEM to verify possible changes in the hydrogels' structure.

2.2.7. Characterization of the degradation profile

The degradation profile of the samples was analyzed in Tris-HCL (pH 5 and pH 8) after incubation at 37 °C under stirring (60 rpm) [28]. After 1, 3, and 7 days, the samples were removed from the Tris-HCL, dried, and weighed. The weight loss percentage was then calculated, at each time point, through Eq. (6):

$$\text{Weight loss (\%)} = \frac{W_i - W_t}{W_i} \times 100 \quad (6)$$

where W_i corresponds to the initial weight of the samples and W_t to the weight of the samples at time t.

2.2.8. Determination of water vapor transmission rate (WVTR)

The WVTR of AWD_100 and AWD_200 was determined following a protocol described elsewhere [2]. Briefly, the AWD ($n = 5$) was used to seal the opening of glass test tubes (1.77 cm^2) containing 10 mL of ultrapure water and incubated at 37 °C. At predetermined incubation times, the amount of evaporated water was measured by weighing the tubes. The WVTR of AWD was then determined through Eq. (7):

$$\text{WVTR} = \frac{W_{loss}}{A} \quad (7)$$

where W_{loss} is the daily weight loss of water and A is the area of the tube opening.

2.2.9. Evaluation of the wettability

The water contact angles of the samples were measured in a Dataphysics OCA 20 contact angle analyzer (Dataphysics Instruments, Filderstadt, Germany) using the sessile drop method. Briefly, a drop of deionized water (10 μL) was automatically dispensed onto the samples' surface and the resultant contact angle was measured. This analysis was performed in ten different regions of the sample for determining the mean static contact angle and its standard error.

2.2.10. Characterization of the biological properties

2.2.10.1. Characterization of cell viability and proliferation. The biocompatibility of the PCL_CA membrane and CS_rGO hydrogels was characterized using the MTS assay, according to ISO 10993-5:2009 (Biological evaluation of medical devices- Part 5: Tests for *in vitro* cytotoxicity) [28]. For that purpose, NHDF cells were seeded at a density of 1 × 10^4 cells/well into 96-well plates and incubated in a 5 % CO_2 humidified atmosphere, at 37 °C, for 24 h. Then, the PCL_CA or CS_rGO samples ($n = 5$, sizes inferior to 10 % of the well's area) were sterilized under UV irradiation (254 nm, ≈ 7 mW/cm^2) for 1 h and incubated with the NHDF cells. After 1 and 3 days of incubation, the medium of each well was replaced by a mixture of 100 μL of fresh culture medium and 20 μL of MTS/phenazine methosulfate (PMS) reagent solution. Then, the plate was incubated for 4 h and the absorbance of each sample was measured at 490 nm using a microplate reader (Biorad xMark microplate spectrophotometer). Cells incubated with EtOH (70 %) were used as the positive control (K^+), while cells incubated only with culture medium were used as the negative control (K^-).

Similarly, the impact of NIR laser irradiation and heat generation in the NHDF cells was also studied. For that purpose, following the addition of the samples, the wells were irradiated with a NIR laser (808 nm, 1.7 W/cm^2), for 10 min after 0 h, 24 h, and 48 h of incubation. Additionally, as a control, NHDF cells non-incubated with materials were also irradiated. Then, the NHDF cellular viability was determined by using the MTS assay, as described above.

2.2.10.2. Confocal microscopic analysis. The cell distribution and adhesion within the hydrogels were characterized through confocal laser scanning microscopy (CLSM). Briefly, NHDF cells (4×10^4 cells/well) were seeded in the presence of CS_rGO hydrogels in μ-Slide 8-well Ibidi imaging plates (Ibidi GmbH, Germany) [2]. After 72 h, the samples were treated with Triton X-100, the cells were labeled with PI (15 mM) for 15 min, and washed with PBS. Imaging experiments were then performed in a Zeiss LSM 710 laser scanning confocal microscope (Carl Zeiss SMT Inc., USA), where consecutive z-stacks were acquired. The 3D reconstruction and image analysis were performed in Zeiss Zen 2010 microscopy software.

2.2.11. Characterization of the antimicrobial activity of the produced layers

2.2.11.1. Analysis of the bacterial adhesion to PCL_CA electrospun membrane. The bacteria adhesion to the PCL_CA surface was evaluated using *S. aureus* (gram-positive) and *E. coli* (gram-negative) bacteria as models [2]. For that purpose, transwell systems (Corning Incorporated, USA) were modified with PCL_CA membrane or filter paper (0.22 μm, which was used as control), acting as the interface between the upper and lower chambers. Then, the bacterial suspension (1×10^8 colony forming units (CFU)/mL) was placed in contact with the membrane and filter paper and incubated for 24 h, at 37 °C. The bacteria adhesion to the PCL_CA surface was then characterized by SEM.

2.2.11.2. Characterization of bactericidal activity of the CS_rGO hydrogel. *S. aureus* and *E. coli* were used to evaluate the antimicrobial properties of the CS_rGO hydrogels [30]. Bacterial suspensions (1×10^8 CFU/mL) in culture medium (LB Broth) were added to the different formulations of CS_rGO, in a 96-well plate, and incubated for 48 h, with or without NIR laser irradiation (808 nm, 1.7 W/cm^2, 10 min) at 0 h, 24 h, and 48 h of incubation. Bacteria non-exposed to the hydrogels were used as the negative control (K^-) whereas bacteria cultured with antibiotics were used as the positive control (K^+). Then, the media was removed and 20 μL of resazurin (0.05 %) were incubated for 4 h. The bacteria viability was determined by measuring the resorufin fluorescence ($\lambda_{ex} = 545$ nm and $\lambda_{em} = 590$ nm) using Spectramax Gemini EM spectrofluorometer (Molecular Devices LLC, CA, USA).

2.3. Statistical analysis

The statistical analysis of the obtained results was performed using a one-way analysis of variance (ANOVA), with the Newman-Keuls *post hoc* test. A *p*-value lower than 0.05. ($p < 0.05$) was considered statistically significant.

3. Results and discussion

3.1. Characterization of the hydrogels

Herein, AWD composed of a PCL_CA electrospun membrane (as the top layer) and a CS_rGO hydrogel (as the bottom layer) were produced, aiming to mimic the epidermis and dermis layers of the native skin, respectively (see Fig. 1).

The CS_rGO hydrogels were produced by combining a CS/rGO mixture with $NaHCO_3$, which acted as the gelling agent, thus mediating the polymers' gelation *via* ionotropic crosslinking as reported in the literature. Guyot et al. produced catechol-CS hydrogels with a high gelation rate and using $NaHCO_3$ as gelling agent [31]. Similarly, Rogina and collaborators developed a CS-hydroxyapatite-based hydrogel with different concentrations of $NaHCO_3$ and observed that higher concentrations of the gelling agent led to faster gelation times [32].

The rGO was produced using dopamine as the reductant, as previously described by our research group, and selected due to its photothermal properties [27]. The physicochemical characterization of rGO revealed that the nanomaterials have a homogeneous size distribution (Fig. S1A) and exhibit a good NIR absorption capacity (Fig. S1B). Furthermore, the incorporation of the rGO within the hydrogels did not compromise its NIR absorption capacity as can be seen in Fig. S1C.

The gelation capacity of CS_rGO hydrogels was confirmed through the tube inversion test, as can be observed in Fig. 2A. Furthermore, the acquired SEM images revealed that the CS_rGO100 and CS_rGO200 hydrogels display in their interior interconnected pores with an irregular shape. Such porosity is compatible with exudate absorption, mass transfer, as well as cell migration and proliferation. Moreover, it is also reported in the literature that the nanomaterials inclusion in biomaterials, such as wound dressings containing rGO, can lead to a higher porosity and surface roughness, which can be further beneficial for the cell adhesion process [33]. The rheological analysis demonstrated an increase in the viscosity of the CS_rGO100 and CS_rGO200 solutions after ≈ 510 s and ≈ 645 s, respectively (Fig. 2B). Such data confirms the CS_rGO ionotropic gelation and is in agreement with a previous work reported elsewhere [26,34]. Despite the higher gelation time of CS_rGO200 hydrogels, these samples achieved a higher viscosity when compared to the CS_rGO100 formulation. Additionally, the strain, Cstrength, and YM of the CS_rGO100 and CS_rGO200 were characterized after the gelation process (Table 1). The results showed an enhanced mechanical performance of CS_rGO hydrogels with the increase of rGO content. In our data, the CS_rGO200 demonstrated a strain of 52.71 ± 4.96 %, a Cstrength of 86.94 ± 10.28 kPa, and a YM of 156.99 ± 9.76 kPa, while the CS_rGO100 presented values of 54.01 ± 6.72 %, 69.08 ± 4.76 kPa and 119.21 ± 9.89 kPa, respectively. In a previous study, Khalili and collaborators developed a CS hydrogel incorporating poly (phenylene sulfide)/rGO that showed a compressive modulus of ≈ 38–49 kPa, depending on the concentration incorporated [35]. Similarly, Kosowska et al. produced a hydrogel modified with rGO and presented a Cstrength of 88.79 ± 8.33 kPa and 15.02 ± 3.21 kPa, with and without rGO, respectively [36].

3.2. Photothermal capacity

The potential of CS_rGO hydrogels for photothermal applications was evaluated by monitoring the temperature changes upon NIR laser irradiation (Fig. 2C). The CS_rGO100 and CS_rGO200 hydrogels after 10

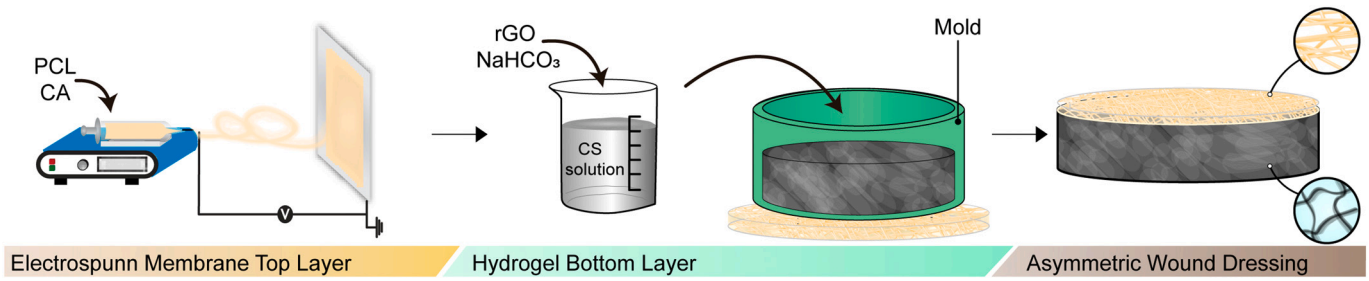

Fig. 1. Scheme of the prodution of the asymmetric wound dressing.

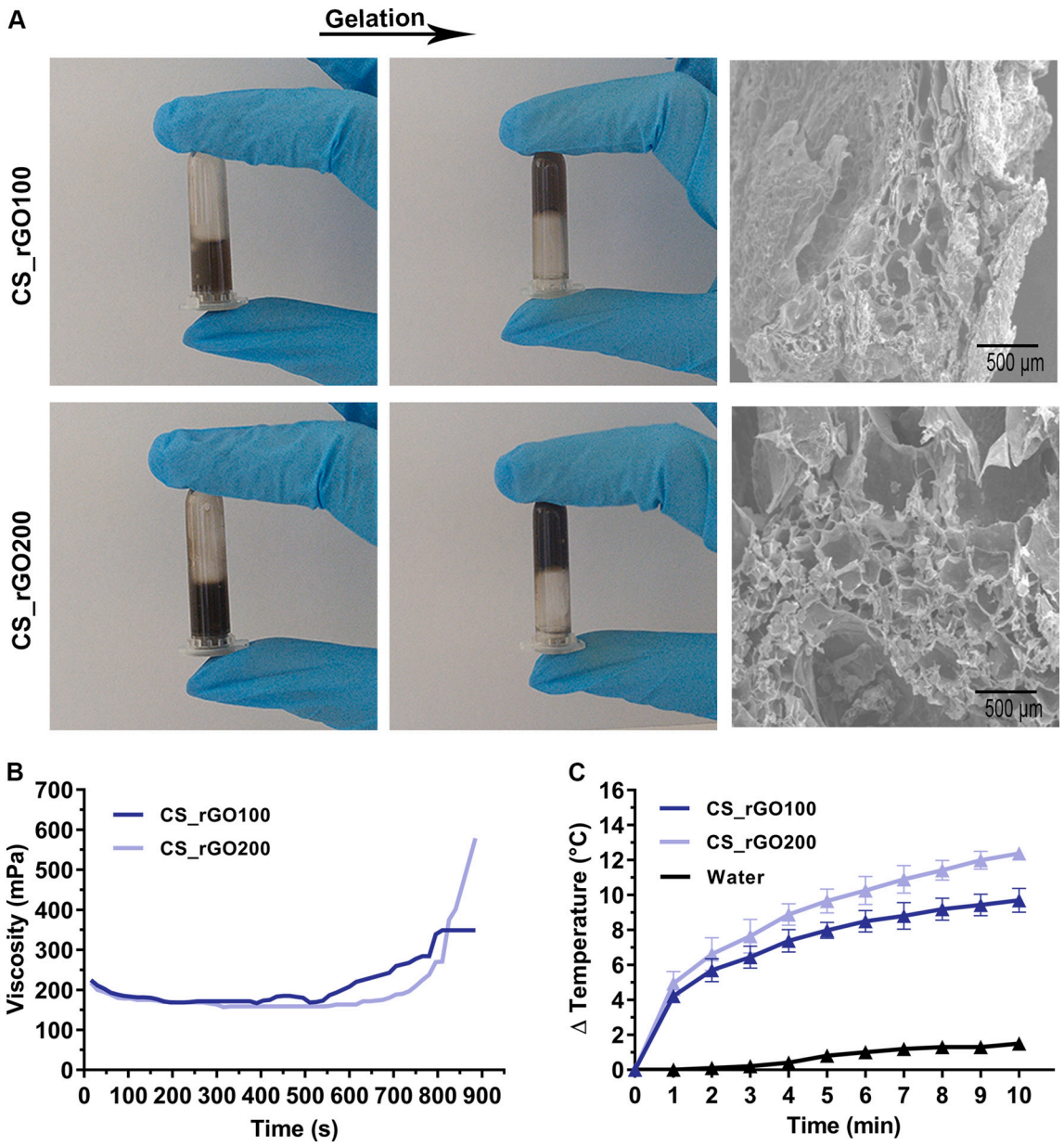

Fig. 2. Characterization of the CS_rGO hydrogel gelation. Macroscopic images of the CS_rGO100 and CS_rGO200 gelation, confirmed by the tube inversion test, and representative SEM images (A). Analysis of the CS_rGO viscosity in the function of the time (constant speed of 60 rpm) (B). Temperature variation curves of the CS_rGO hydrogels during NIR light irradiation (808 nm, 1.7 W/cm^2, 10 min) (C).

Table 1
Mechanical properties of the different hydrogels.

Samples	Strain (%)	Cstrength (kPa)	YM (kPa)
CS_rGO100	54.01 ± 6.72	69.08 ± 4.76	119.21 ± 9.89
CS_rGO200	52.71 ± 4.96	86.94 ± 10.28	156.99 ± 9.76

min of irradiation with a NIR laser (808 nm, 1.7 W/cm^2), exhibited a 9.7 ± 0.7 °C and 12.4 ± 0.3 °C increase in their surface temperatures, respectively. Therefore, the results demonstrate that a higher rGO content in the hydrogel leads to an higher temperature increase. Nevertheless, both CS_rGO hydrogels were able to mediate a mild hyperthermic effect that can be explored to improve the wound healing process without damaging the cells [17,18,20]. In a previous study, Li et al. developed hydrogels based on quaternized CS, polydopamine-coated rGO and poly(*N*-isopropylacrylamide) with different concentrations of GO (1, 2, 3, and 4 mg/mL) [37]. These hydrogels achieved a temperature increase of 9.6, 10.8, 12.1, and 12.6 °C after 10 min of NIR irradiation (808 nm, 1.0 W/cm^2), using different concentrations of GO (1, 2, 3, and 4 mg/mL, respectively). Herein, a similar temperature increase was attained using a lower concentration of the photothermal agent and a slightly higher NIR light intensity.

3.3. Characterization of the surface morphology and composition

SEM analyses were performed to characterize the morphology of both layers of the AWD (Fig. 3). The SEM images showed that the electrospun membrane has a 3D nanofibrous mesh with a mean diameter of 615.12 ± 139.47 nm, composed of randomly oriented and non-beaded fibers (Fig. 3A). The structural organization and fiber size presented by the produced membrane is in accordance with previous works, where PCL or CA nanofibrous membranes were also produced. Ren et al. obtained PCL/Gel nanofibers with an average diameter of ≈ 600 nm

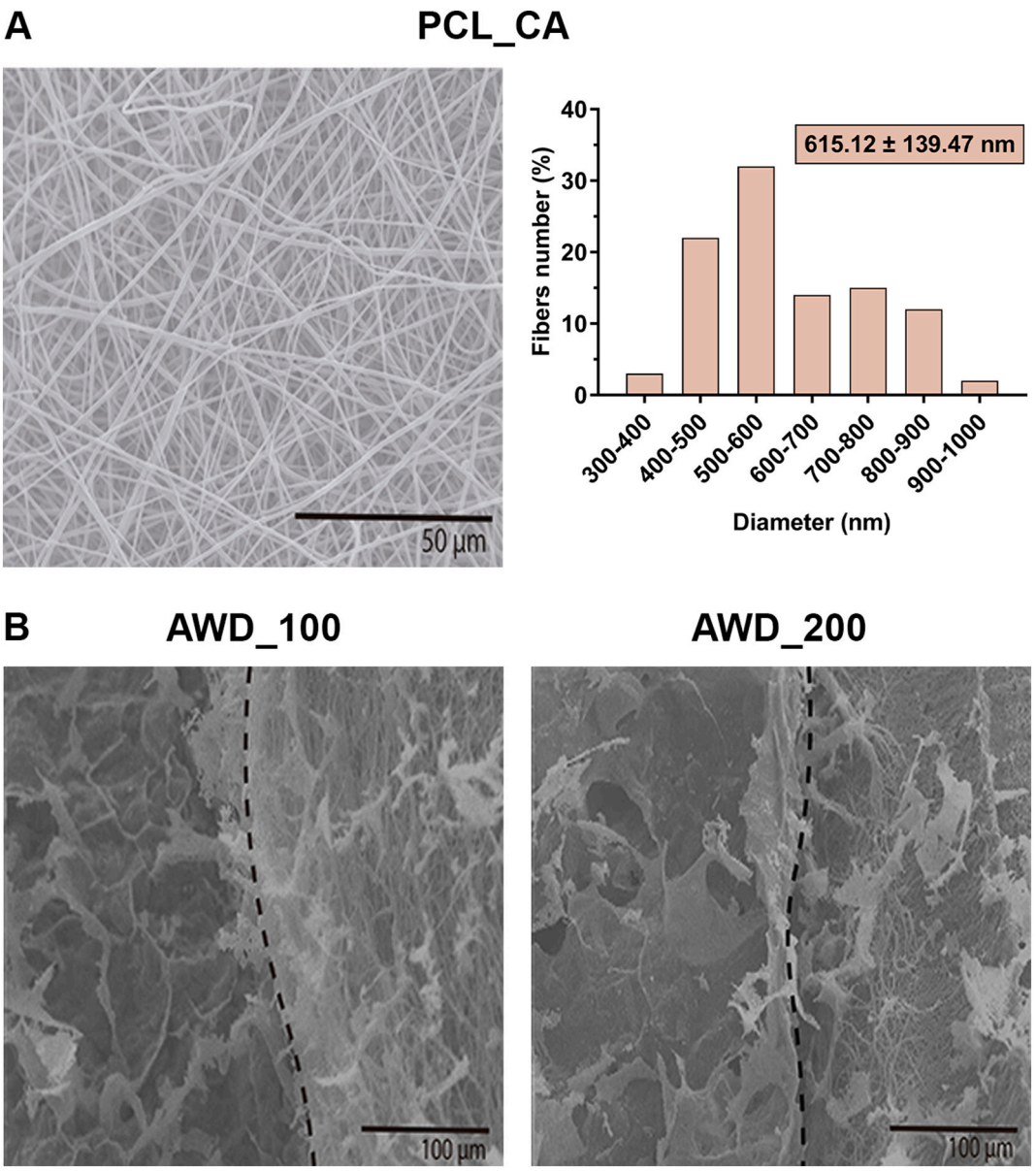

Fig. 3. Characterization of the PCL_CA and AWD morphological properties. Representative SEM image and fibers' size distribution analysis of the PCL_CA membrane (A). Representative SEM images of the cross-section images of AWD_100 and AWD_200 (B).

[38]. Quirós et al. produced CA electrospun membranes with a mean fiber diameter of 593 nm [39]. Moreover, the layered structure as well as the interconnection between the layers of the AWD were also observed (Fig. 3B).

The chemical composition of both PCL_CA and CS_rGO layers was confirmed by FTIR. The PCL_CA spectrum (Fig. 4A) exhibits the characteristic peaks of PCL at 2940 cm^{-1} (CH_2 stretching), 1724 cm^{-1} (C═O stretching), and 1170 cm^{-1} (C-O-C stretching) [40]. In addition, the characteristic peaks of CA were also observed at 1731 cm^{-1} (C═O stretching), 1370 cm^{-1} (CH_3 stretching), and 1226 cm^{-1} (C-O-C stretching) [41]. Otherwise, both the CS_rGO100 and CS_rGO200 spectra (Fig. 4B) display the characteristic peaks of CS at 1025 cm^{-1}

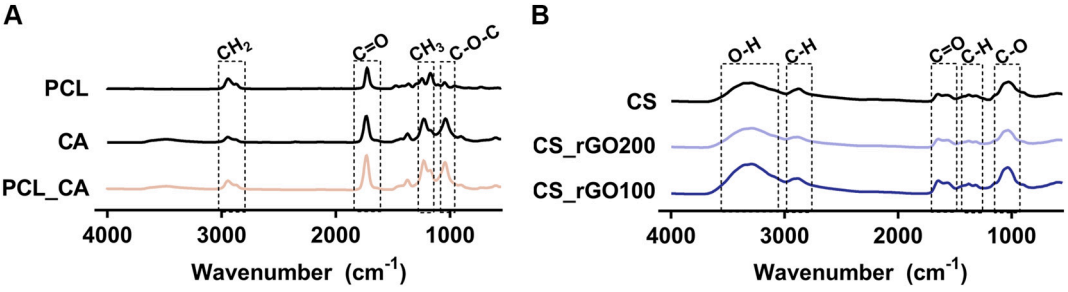

Fig. 4. ATR-FTIR spectra of the PCL_CA membrane (A) and CS_rGO hydrogels (B) as well as their respective raw polymeric materials.

(C—O stretching), 1374 cm^{-1} (C—H symmetrical bending), 1646 cm^{-1} (C=O-NHR band), 2873 cm^{-1} (C—H stretching vibrations) and 3292 cm^{-1} (O—H vibrations) [42]. Therefore, the FTIR spectra of each layer show the characteristic peaks of the raw materials, revealing that the production methodology did not compromise the chemical composition of the polymers.

3.4. Evaluation of asymmetric wound dressing's porosity

The porosity of the wound dressings enables cell migration, gas exchange, nutrient supply, and fluid loss control, required for an enhanced wound-healing process to occur [43,44]. Herein, the PCL_CA membrane displayed an overall porosity of 81.41 ± 5.20 %, which is within the ideal range described in the literature (60–90 %) for wound healing purposes [44]. Moreover, a dense and compact nanofibrous structure may be important for preventing bacterial penetration (Fig. 3A).

In turn, CS_rGO hydrogels' SEM images present a highly porous structure with large pores (see further details in Fig. 2A). Additionally, after immersion of CS_rGO hydrogels in Tris-HCl at pH 5 and pH 8, for 7 days, it was observed that the pore size increase when the hydrogels were incubated at pH 5 (Fig. 5A). Such can be justified by the pKa of 6–6.5 of the amino groups present in the CS backbone, which are in a protonated state at pH 5, thus enabling the swelling of the polymeric matrix, leading to an increased porosity [45].

3.5. Characterization of the swelling profile

Wound humidity control is crucial for the wound healing process as well as for preventing bacterial infection [46]. In this way, an ideal wound dressing must be able to absorb the excessive exudate, which contributes for tissue maceration and the occurrence of infections [47]. In this study, the absorption capacity of the AWD samples was analyzed through their incubation in Tris-HCL, at pH 5 and pH 8 (Fig. 5B and C, respectively), for 8 days. The results showed that the AWD_100 and AWD_200 presented a swelling ratio of 1.13 and 1.01, at pH 5 and 0.72 and 0.80 at pH 8, respectively. The higher swelling at pH 5 can be explained by the protonation state of the CS's amino groups present in the hydrogels. At acidic pH, the CS is protonated (*i.e.*, positively charged) and presents an increased solubility in water. However, at pH > 6–6.5, the amino groups of CS are deprotonated decreasing the polymer solubility [45]. This behavior is in accordance with several works reporting CS-based hydrogels [48,49]. Furthermore, Wsoo and collaborators also developed a PCL_CA electrospun membrane loaded with vitamin D3 (20%) that displayed a swelling ratio of 91.8 %, after 30 days [50].

3.6. Characterization of the asymmetric wound dressing's biodegradation profile

The degradation percentage exhibited by the wound dressing should match the regeneration rate of native skin [51]. In this way, the degradation frequency was evaluated for 7 days after the materials' incubation in Tris-HCL at pH 5 and pH 8 (Fig. 6A and B, respectively). The PCL_CA membrane presented a weight loss of 14.02 ± 1.18 % and 12.46 ± 6.16 %, at pH 5 and pH 8, respectively. Such results can be explained by the high stability of PCL in aqueous solutions, which can undergo a very slow hydrolytic degradation [52]. Furthermore, CA also presents a slow degradation as demonstrated by Nosar and collaborators, who produced a wet-electrospun CA (7 % of CA) membrane, that presented a weight loss of 16.50 % after 30 days [53].

The CS_rGO100 and CS_rGO200 hydrogels, produced herein, presented a weight loss of 53.53 ± 2.50 % and 48.86 ± 3.57 %, at pH 5, and 48.62 ± 8.39 % and 47.36 ± 4.71 % at pH 8, respectively. These degradation profiles are similar to those reported in previous works. Lima et al. developed hydrogels based on CS and rGO that presented weight loss of ≈ 50 %, after 7 days [27]. Melo et al. reported ≈ 45 % of weight loss for CS_rGO gels, after 5 days [26]. Furthermore, the AWD_100 and AWD_200 presented a weight loss of 40.62 ± 4.0 % and 37.28 ± 3.91 %, at pH 5, and 39.15 ± 2.54 % and 41.65 ± 1.93 % at pH 8, respectively. Such results are coherent with the degradation of the

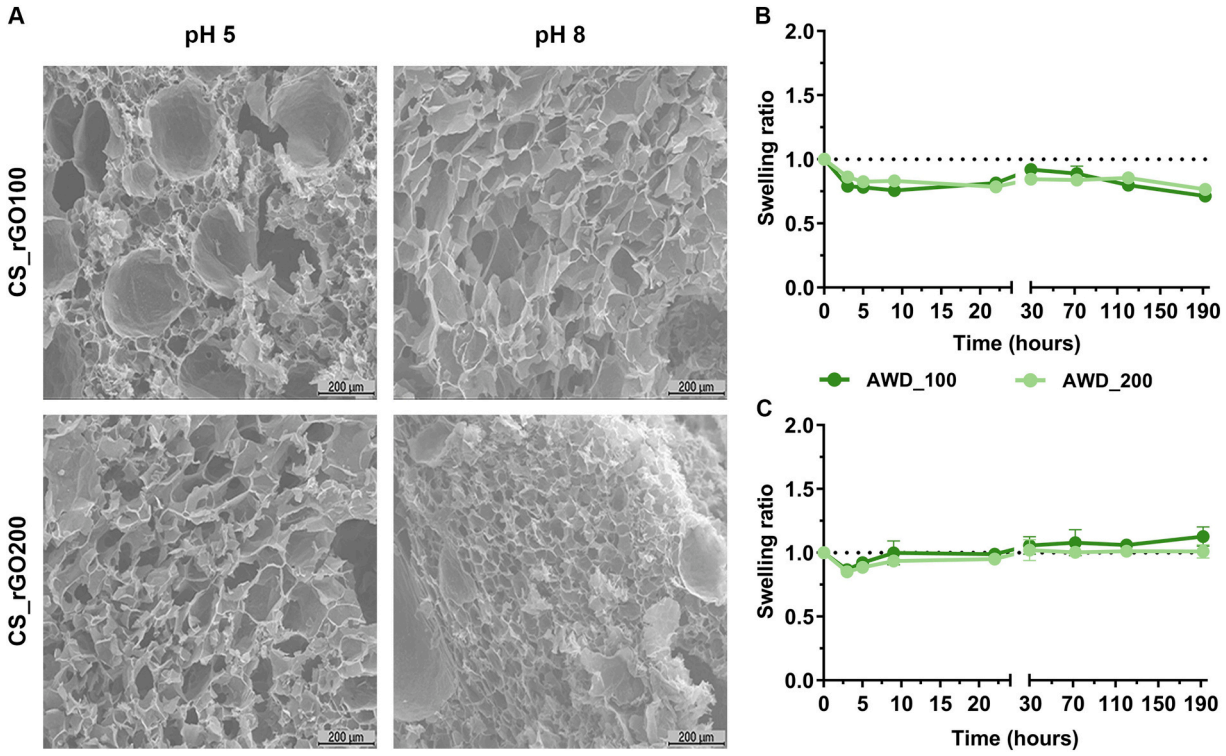

Fig. 5. Characterization of the CS_rGO, PCL_CA, and AWD swelling behavior. Representative SEM images of the CS_rGO100 and CS_rGO200 cross-sections after 7 days of immersion in Tris-HCl at pH 5 and pH 8 (A). Analysis of the AWD_100 and AWD_200 swelling profile at pH 5 (B) and pH 8 (C).

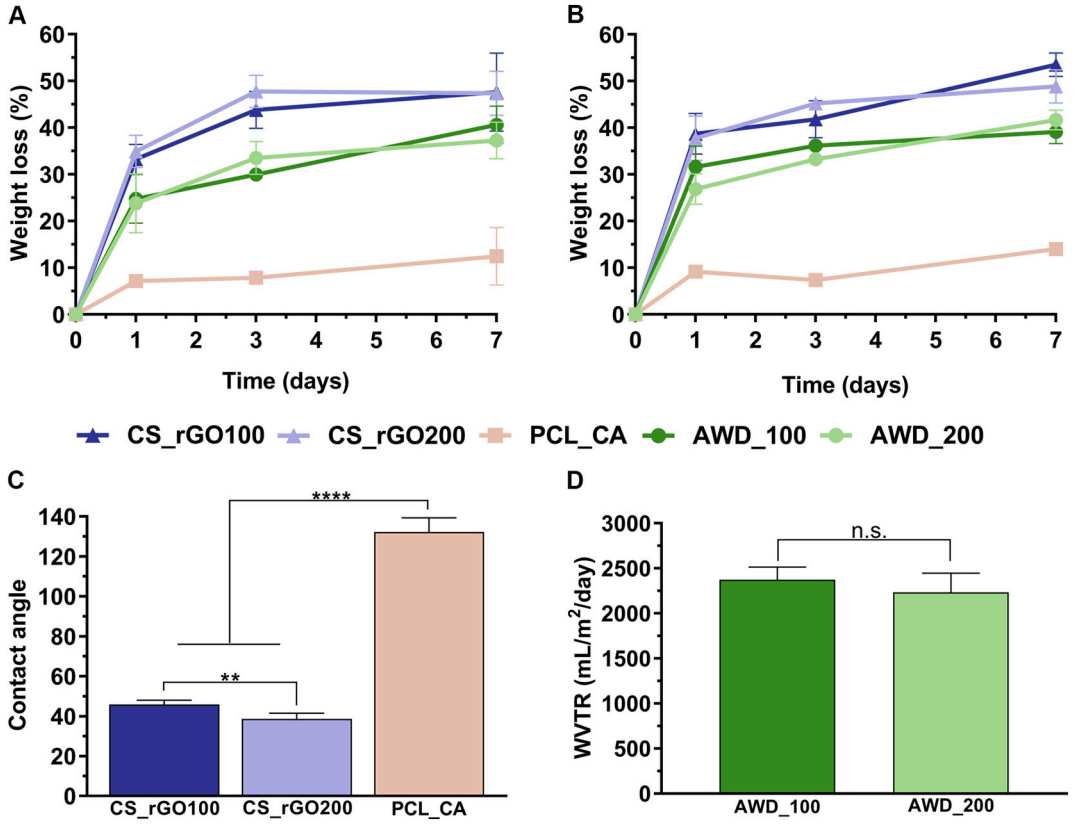

Fig. 6. Characterization of CS_rGO, PCL_CA, and AWD physicochemical properties. Determination of the weight losses after 1, 3, and 7 days, at pH 5 (A) and pH 8 (B). Analysis of the WCA (C) and WVTR values (D). Data are presented as the mean ± standard deviation, $n = 5$, n.s. = non-significant.

principal layer of the AWD, the CS_rGO layer.

3.7. Determination of the asymmetric wound dressing's wettability

The surface wettability of the wound dressings has a direct impact on their biological performance, namely on the capacity of cells to adhere on their surface. The WCA measurements shown in Fig. 6C demonstrate that the PCL_CA membrane has a hydrophobic character, WCA of 132.2 ± 7.2°. Such data is justified by the hydrophobic nature of PCL and CA, which can play an important role in preventing bacterial adhesion to the material's surface [54]. On the other side, the CS_rGO100 and CS_rGO200 hydrogels exhibited a WCA of 45.9 ± 2.1° and 38.7 ± 2.8°, revealing a hydrophilic surface (10° < WCA < 90°) [55]. These results show that the increase in the rGO content results in materials with hydrophilic character. Nevertheless, such feature of the bottom layer will be important to support the cells' adhesion and promote tissue regeneration [55].

3.8. Determination of the water vapor transmission rate

The WVTR of a wound dressing also impacts on wound hydration. An high WVTR can result in wound dehydration and consequent attachment of the dressing, while a low WVTR can cause liquid accumulation and consequent tissue maceration [47]. Fig. 6D shows that the AWD_100 and AWD_200 present WVTR values of 2374.01 ± 140.64 mL/m^2/day and 2232.77 ± 214.63 mL/m^2/day, respectively. These WVTR values are within the recommended range, *i.e.*, 2000–2500 mL/m^2/day, which demonstrates that the produced asymmetric wound dressings are efficient in providing a moist environment, preventing exudate accumulation, and allowing water vapor exchanges [47].

Moreover, the WVTR values displayed by the AWD are higher than those found in commercial wound dressings, *e.g.* Tegasorb (ConvaTec Ltd) presents a WVTR of 136 ± 15 g/m^2/day, while for Bioclusive™ (Johnson-Johnson) the WVTR is 394 ± 12 g/m^2/day, and Comfeel (Coloplast A/S) presents a WVTR value of 285 ± 8 g/m^2/day [56].

3.9. Characterization of biological properties of the produced membranes

The cytocompatibility of CS_rGO and PCL_CA was evaluated using NHDF cells, (as cell model), by optical microscopy and MTS assay. The representative optical microscopy images (Fig. S2) show that NHDF cells did not suffer any morphologic variation after incubation with CS_rGO and PCL_CA. In fact, it is possible to observe that the NHDF cells in the test groups have an elongated morphology similar to that observed in the negative control. Furthermore, the MTS assay confirmed that NHDF cells remained viable, *i.e.*, cell viability is superior to 70 %, after 1 and 3 days of incubation with CS_rGO and PCL_CA (Fig. 7A and B, respectively). Altogether, both optical microscopy and MTS data indicate the good biocompatibility of the PCL_CA electrospun membrane and CS_rGO hydrogels, and their ability to promote the proliferation of fibroblast cells. Furthermore, Fig. 7A and B show that after one or three NIR laser irradiations (808 nm, 1.7 W/cm^2, 10 min), NHDF cells remained viable. Such data further validates the AWD cytocompatibility and the safety of the mild-hyperthermia treatment.

Otherwise, the NHDF cells' adhesion to CS_rGO hydrogels with or without NIR laser irradiation (808 nm, 1.7 W/cm^2, 10 min) was also analyzed by CLSM (Fig. 7C). The fluorescence CLSM images revealed that NHDF cells (red color) adhered to the surface of the CS_rGO100 and CS_rGO200 hydrogels and proliferated. In addition, no negative effects were noticed after the NIR laser irradiation. Such results further corroborate the biocompatibility of the AWD layers and their capacity to act as temporary support for cell adhesion and growth, processes that are fundamental to stimulating the wound healing process.

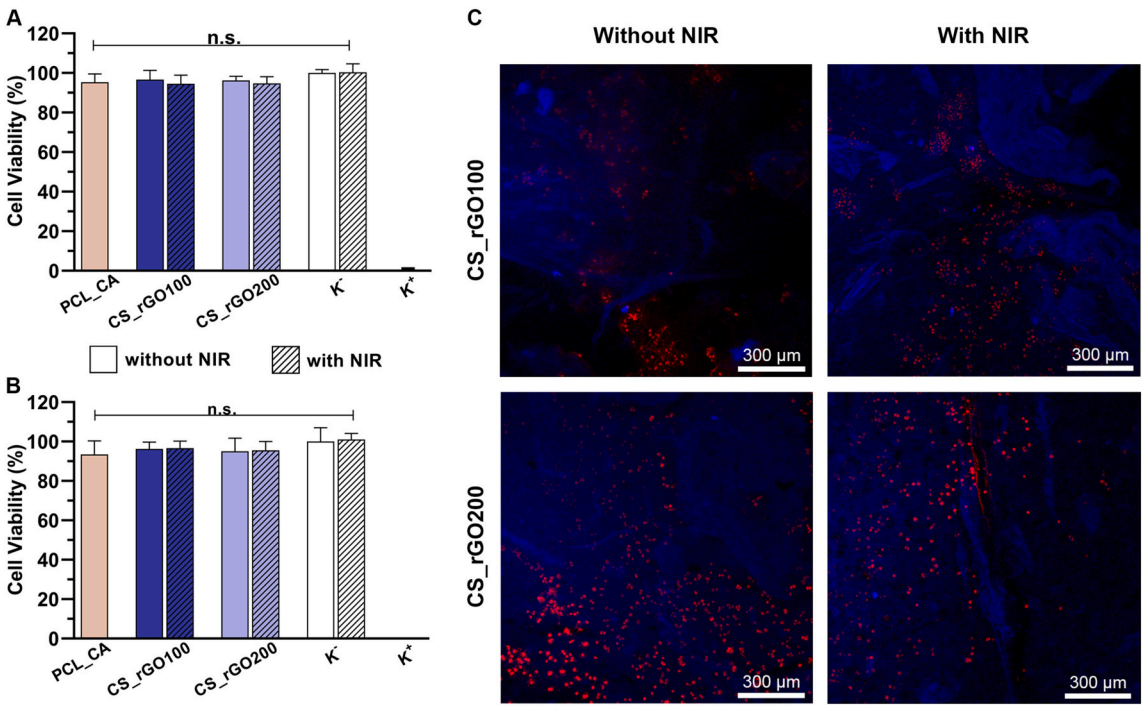

Fig. 7. Evaluation of the asymmetric wound dressings' cytocompatibility. Analysis of the NHDF cellular viability after 1 (A) and 3 days (B) of contact with PCL_CA membrane, CS_rGO100, and CS_rGO200 hydrogels with or without NIR irradiation (808 nm, 1.7 W/cm^2, 10 min), through MTS. K^- (live cells); K^+ (dead cells). Data are presented as the mean ± standard deviation, n = 5, n.s. = non-significant. CLSM images of NHDF cells (stained with PI – red channel) after incubation with CS_rGO100 and CS_rGO200 hydrogels (materials autofluorescence - blue channel), with or without NIR irradiation (808 nm, 1.7 W/cm^2, 10 min) (C).

3.10. Antibacterial properties

Skin and soft tissue infections have a high incidence and associated morbidity. Upon disruption of skin integrity, the occurrence of infections will impair the wound-healing process. These infections can be caused by different bacteria, *i.e.*, in the initial stages infections occur

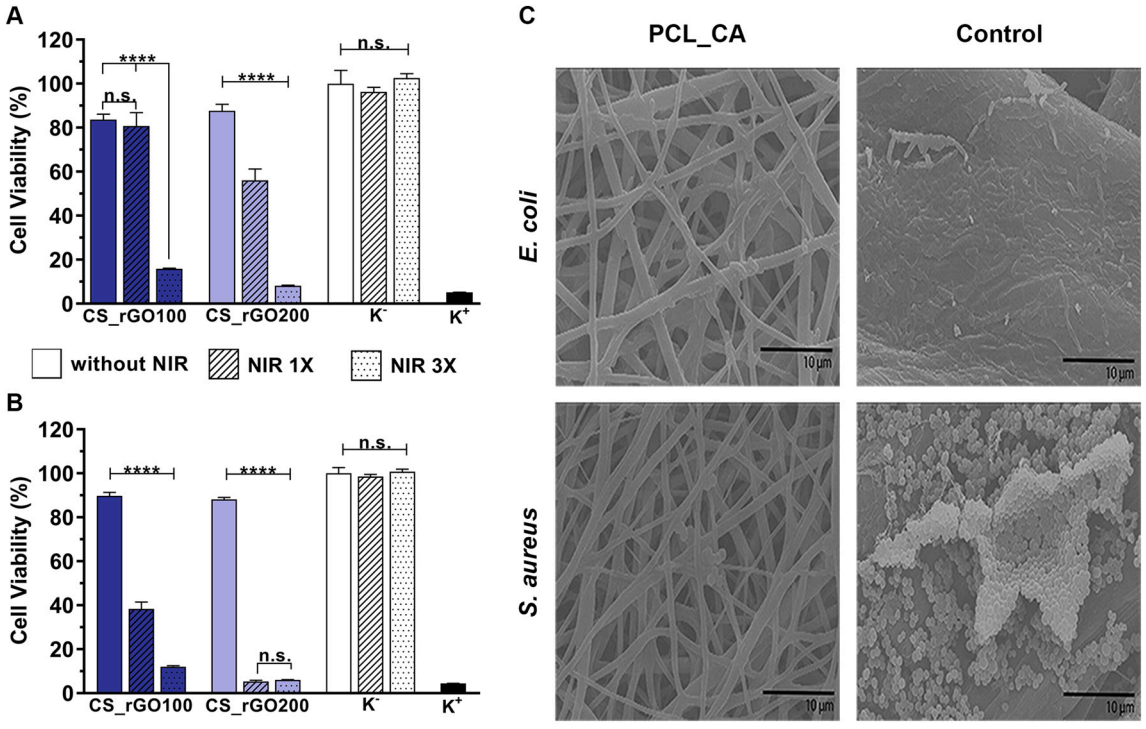

Fig. 8. Determination of the antibacterial potential of the CS_rGO and PCL_CA. Analysis of the *E. coli* (A) and *S. aureus* (B) viability after 24 h and 48 h of contact with CS_rGO100 and CS_rGO200 solutions, with or without NIR irradiation (808 nm, 1.7 W/cm^2, 10 min) (K^- (live bacteria); K^+ (dead bacteria)). Data are presented as the mean ± standard deviation, n = 5, ****$p < 0.0001$. Representative SEM images of the surface of the PCL_CA electrospun membrane after incubation with *S. aureus* and *E. coli* (C).

mainly as a consequence of gram-positive bacteria, such as *S. aureus*, while in later stages they are principally associated with gram-negative bacteria, such as *E. coli* and *Pseudomonas aeruginosa* [13,57]. In this way, the antibacterial properties of CS_rGO100 and CS_rGO200 hydrogels were analyzed using both *S. aureus* and *E. coli* bacteria, with or without NIR laser irradiation (808 nm, 1.7 W/cm^2, 10 min) (Fig. 8A and B). The obtained results showed that after incubation with CS_rGO100 and CS_rGO200 hydrogels without NIR irradiation, most of the bacteria remained viable (84 % and 88 % for *E. coli* and 90 % and 88 % for *S. aureus*, respectively). Besides, after a single NIR irradiation (808 nm, 1.7 W/cm^2, 10 min) of CS_rGO100 and CS_rGO200 hydrogels, the bacteria viability decreased to 81 % and 56 % for *E. coli* and to 38 % and 5 % for *S. aureus*, respectively. This antibacterial effect was further enhanced with three cycles of NIR laser irradiation (808 nm, 1.7 W/cm^2, 10 min). The viability of *E. coli* decreased to 16 % and 8 %, and to 12 % and 6 % for *S. aureus*. These results demonstrated that NIR laser irradiation improves the antibacterial properties of the hydrogels. Such effect can be explained by the bacteria death in response to the temperature increase [27]. Additionally, the temperature increase may also promote the dissolution of CS, increasing its interaction with bacteria and therefore enhance the hydrogel's antibacterial properties [27,58]. The antibacterial activity of CS is mostly related to the amino groups ($-NH_2$) present in its chemical structure [13,59,60]. One of the mechanisms proposed to explain the CS' antibacterial activity comprises the interaction between the positively charged (NH_2) groups on the polymeric backbone and the negatively charged components (*e.g.*, peptidoglycans) at the bacterial cell wall [59]. Moreover, research data also indicate that CS may also interact with essential trace metals and oligo-elements, mediating the production of toxins and inhibiting microbial growth, or form a polymeric envelope around bacteria, inhibiting nutrients' absorption and intercellular exchanges [13,59,61,62].

Furthermore, the results also showed that *S. aureus* bacteria was more sensible to the combination of the hydrogel incubation with the NIR irradiation. This result can be explained by the differences observed in the cell wall structure of gram-negative and gram-positive bacteria [27]. Apart from the antibacterial properties of the CS_rGO bottom layer, the PCL_CA electrospun membrane should also act as a protective barrier that avoids microbial invasion of the wound site. The SEM images of PCL_CA electrospun membrane incubated with *S. aureus* and *E. coli* bacteria (Fig. 8C) showed a very small number of adhered bacteria when compared to the control group (*i.e.*, filter paper with a pore size of 0.22 μm), due to its hydrophobic character. Altogether, these results highlight the antibacterial potential of the AWD, particularly by providing simultaneously a barrier against bacteria access to the wound site and a NIR-triggered antibacterial effect.

4. Conclusions and Future Perspectives

Acute and chronic skin injuries are still considered a major health issue for the worldwide population. The current clinical therapeutic strategies present some limitations, and none of them is capable of fully restoring the structure and functions of the native skin. Therefore, asymmetric wound dressings have captured the attention of researchers, due to their capacity to mimic the layered structure of the skin. Moreover, researchers have also been exploring the potential of NIR-activated photothermal therapies aimed for the treatment of infections as well as a complement to improve the wound healing process.

Herein, an asymmetric wound dressing was produced combining a CS_rGO hydrogel and an electrospun PCL_CA membrane, mimicking the dermis and epidermis layers of the skin, respectively. The top layer (PCL_CA membrane) presented a low porosity and hydrophobic character, which was essential to provide a protective barrier against external harmful agents. On the other side, the bottom layer (CS_rGO hydrogel) displayed responsiveness to NIR, due to the presence of rGO, which improved dressing antibacterial properties against *E. coli* and *S. aureus*. In this way, the AWD shows the potential to prevent or treat skin infections due to its capacity to act as a barrier against bacteria access to the wound site and as a NIR-triggered antibacterial agent. Moreover, the AWD also presented physicochemical properties compatible with the maintenance of a favorable environment that promotes the healing process. Additionally, the *in vitro* assays revealed that the AWD can act as a support for the adhesion and growth of human fibroblasts, even under the NIR irradiation cycles.

In the near future, bioactive molecules (*e.g.,* vitamins, proteins, or growth factors) will be incorporated in AWD to enhance other important biological properties, *e.g.* modulation of the inflammatory response, reactive oxygen species generation, as well as cell differentiation and proliferation. Furthermore, *in vivo* assays are aimed to be performed in order to validate the AWD and mild-hyperthermy potential for accelerating the wound healing process.

CRediT authorship contribution statement

Mariana F. Graça: Conceptualization, Methodology, Investigation, Writing - Original Draft. Bruna L. Melo: Methodology, Investigation. Rita Lima-Sousa: Methodology, Investigation. Paula Ferreira: Investigation, Visualization. André F. Moreira: Methodology, Investigation, Writing - Original Draft, Writing- Reviewing and Editing. Ilídio J. Correia: Conceptualization, Writing- Reviewing and Editing, Funding acquisition.

Declaration of competing interest

The authors declare the following financial interests/personal relationships which may be considered as potential competing interests: Mariana F. P. Graca reports financial support was provided by Foundation for Science and Technology. Bruna L. Melo reports financial support was provided by Foundation for Science and Technology. Rita Lima-Sousa reports financial support was provided by Foundation for Science and Technology. Andre F. Moreira reports financial support was provided by Foundation for Science and Technology. Ilidio J. Correia reports financial support was provided by Foundation for Science and Technology. Andre F. Moreira reports financial support was provided by Fundo Europeu de Desenvolvimento Regional. Ilidio J. Correia reports financial support was provided by Fundo Europeu de Desenvolvimento Regional.

Data availability

Data will be made available on request.

Acknowledgments

This work was financed by the Foundation for Science and Technology (FCT), through funds from the State Budget, and by the European Regional Development Fund (ERDF), under the Portugal 2020 Program, through the Regional Operational Program of the Center (Centro2020), through the Project with the reference UIDB/00709/2020. The funding from CENTRO-01-0145-FEDER-028989 and POCI-01-0145-FEDER-031462 are also acknowledged. Mariana F. P. Graça, Bruna L. Melo and Rita Lima-Sousa acknowledge funding from individual Ph.D. fellowships from FCT (2021.08657.BD, 2021.06044.BD and SFRH/BD/144922/2019).

Appendix A. Supplementary data

Supplementary data to this article can be found online at https://doi.org/10.1016/j.ijbiomac.2022.12.291.

References

[1] E. Rezvani Ghomi, S. Khalili, S. Nouri Khorasani, R. Esmaeely Neisiany, S. Ramakrishna, Wound dressings: current advances and future directions, J. Appl. Polym. Sci. 136 (27) (2019) 47738.

[2] S.P. Miguel, C.S. Cabral, A.F. Moreira, I.J. Correia, Production and characterization of a novel asymmetric 3D printed construct aimed for skin tissue regeneration, Colloids Surf. B: Biointerfaces 181 (2019) 994–1003.

[3] B. Yu, C. He, W. Wang, Y. Ren, J. Yang, S. Guo, Y. Zheng, X. Shi, Asymmetric wettable composite wound dressing prepared by electrospinning with bioinspired micropatterning enhances diabetic wound healing, ACS Appl. Bio Mater. 3 (8) (2020) 5383–5394.

[4] J. Liu, Z. Qian, Q. Shi, S. Yang, Q. Wang, B. Liu, J. Xu, X. Guo, H. Liu, An asymmetric wettable chitosan–silk fibroin composite dressing with fixed silver nanoparticles for infected wound repair: in vitro and in vivo evaluation, RSC Adv. 7 (69) (2017) 43909–43920.

[5] R. Eivazzadeh-Keihan, F. Ahmadpour, H.A.M. Aliabadi, F. Radinekiyan, A. Maleki, H. Madanchi, M. Mahdavi, A.E. Shalan, S. Lanceros-Méndez, Pectin-cellulose hydrogel, silk fibroin and magnesium hydroxide nanoparticles hybrid nanocomposites for biomedical applications, Int. J. Biol. Macromol. 192 (2021) 7–15.

[6] R. Eivazzadeh-Keihan, H.A.M. Aliabadi, F. Radinekiyan, M. Sobhani, A. Maleki, H. Madanchi, M. Mahdavi, A.E. Shalan, Investigation of the biological activity, mechanical properties and wound healing application of a novel scaffold based on lignin–agarose hydrogel and silk fibroin embedded zinc chromite nanoparticles, RSC Adv. 11 (29) (2021) 17914–17923.

[7] R. Eivazzadeh-Keihan, F. Khalili, H.A.M. Aliabadi, A. Maleki, H. Madanchi, E. Z. Ziabari, M.S. Bani, Alginate hydrogel-polyvinyl alcohol/silk fibroin/magnesium hydroxide nanorods: a novel scaffold with biological and antibacterial activity and improved mechanical properties, Int. J. Biol. Macromol. 162 (2020) 1959–1971.

[8] R. Eivazzadeh-Keihan, F. Radinekiyan, H.A.M. Aliabadi, S. Sukhtezari, B. Tahmasebi, A. Maleki, H. Madanchi, Chitosan hydrogel/silk fibroin/Mg (OH) 2 nanobiocomposite as a novel scaffold with antimicrobial activity and improved mechanical properties, Sci. Rep. 11 (1) (2021) 1–13.

[9] R. Eivazzadeh-Keihan, F. Radinekiyan, A. Maleki, M.S. Bani, Z. Hajizadeh, S. Asgharnasl, A novel biocompatible core-shell magnetic nanocomposite based on cross-linked chitosan hydrogels for in vitro hyperthermia of cancer therapy, Int. J. Biol. Macromol. 140 (2019) 407–414.

[10] A. Maleki, Green oxidation protocol: selective conversions of alcohols and alkenes to aldehydes, ketones and epoxides by using a new multiwall carbon nanotube-based hybrid nanocatalyst via ultrasound irradiation, Ultrason. Sonochem. 40 (2018) 460–464.

[11] A. Maleki, M. Aghaie, Ultrasonic-assisted environmentally-friendly synergetic synthesis of nitroaromatic compounds in core/shell nanoreactor: a green protocol, Ultrason. Sonochem. 39 (2017) 534–539.

[12] J. Rahimi, R. Taheri-Ledari, M. Niksefat, A. Maleki, Enhanced reduction of nitrobenzene derivatives: effective strategy executed by Fe3O4/PVA-10% ag as a versatile hybrid nanocatalyst, Catal. Commun. 134 (2020), 105850.

[13] D. Simões, S.P. Miguel, M.P. Ribeiro, P. Coutinho, A.G. Mendonça, I.J. Correia, Recent advances on antimicrobial wound dressing: a review, Eur. J. Pharm. Biopharm. 127 (2018) 130–141.

[14] Y. Liu, B. Xu, M. Lu, S. Li, J. Guo, F. Chen, X. Xiong, Z. Yin, H. Liu, D. Zhou, Ultrasmall fe-doped carbon dots nanozymes for photoenhanced antibacterial therapy and wound healing, Bioact. Mater. 12 (2022) 246–256.

[15] X. Gao, M. Wei, D. Ma, X. Yang, Y. Zhang, X. Zhou, L. Li, Y. Deng, W. Yang, Engineering of a hollow-structured Cu2− XS nano-homojunction platform for near infrared-triggered infected wound healing and cancer therapy, Adv. Funct. Mater. 31 (52) (2021), 2106700.

[16] X. Chu, P. Zhang, Y. Wang, B. Sun, Y. Liu, Q. Zhang, W. Feng, Z. Li, K. Li, N. Zhou, Near-infrared carbon dot-based platform for bioimaging and photothermal/photodynamic/quaternary ammonium triple synergistic sterilization triggered by single NIR light source, Carbon 176 (2021) 126–138.

[17] X. Yi, Q.-Y. Duan, F.-G. Wu, Low-temperature photothermal therapy: strategies and applications, Research 2021 (2021).

[18] X. Xu, X. Liu, L. Tan, Z. Cui, X. Yang, S. Zhu, Z. Li, X. Yuan, Y. Zheng, K.W. K. Yeung, Controlled-temperature photothermal and oxidative bacteria killing and acceleration of wound healing by polydopamine-assisted au-hydroxyapatite nanorods, Acta Biomater. 77 (2018) 352–364.

[19] L. Sheng, Z. Zhang, Y. Zhang, E. Wang, B. Ma, Q. Xu, L. Ma, M. Zhang, G. Pei, J. Chang, A novel "hot spring"-mimetic hydrogel with excellent angiogenic properties for chronic wound healing, Biomaterials 264 (2021), 120414.

[20] Y. Huang, Q. Gao, X. Li, Y. Gao, H. Han, Q. Jin, K. Yao, J. Ji, Ofloxacin loaded MoS2 nanoflakes for synergistic mild-temperature photothermal/antibiotic therapy with reduced drug resistance of bacteria, Nano Res. 13 (9) (2020) 2340–2350.

[21] G. Reina, J.M. González-Domínguez, A. Criado, E. Vázquez, A. Bianco, M. Prato, Promises, facts and challenges for graphene in biomedical applications, Chem. Soc. Rev. 46 (15) (2017) 4400–4416.

[22] X. Zhang, B. Tan, Y. Wu, M. Zhang, X. Xie, J. Liao, An injectable, self-healing carboxymethylated chitosan hydrogel with mild photothermal stimulation for wound healing, Carbohydr. Polym. 293 (2022), 119722.

[23] W. Han, Z. Wu, Y. Li, Y. Wang, Graphene family nanomaterials (GFNs)—promising materials for antimicrobial coating and film: a review, Chem. Eng. J. 358 (2019) 1022–1037.

[24] S. Mukherjee, P. Sriram, A.K. Barui, S.K. Nethi, V. Veeriah, S. Chatterjee, K. I. Suresh, C.R. Patra, Graphene oxides show angiogenic properties, Adv. Healthc. Mater. 4 (11) (2015) 1722–1732.

[25] I.A. Zárate, H. Aguilar-Bolados, M. Yazdani-Pedram, G.D.C. Pizarro, A. Neira-Carrillo, In Vitro hyperthermia evaluation of electrospun polymer composite fibers loaded with reduced graphene oxide, Polymers 12 (11) (2020) 2663.

[26] B.L. Melo, R. Lima-Sousa, C.G. Alves, A.F. Moreira, I.J. Correia, D. de Melo-Diogo, Chitosan-based injectable in situ forming hydrogels containing dopamine-reduced graphene oxide and resveratrol for breast cancer chemo-photothermal therapy, Biochem. Eng. J. 185 (2022), 108529.

[27] R. Lima-Sousa, D. de Melo-Diogo, C.G. Alves, C.S. Cabral, S.P. Miguel, A. G. Mendonça, I.J. Correia, Injectable in situ forming thermo-responsive graphene based hydrogels for cancer chemo-photothermal therapy and NIR light-enhanced antibacterial applications, Mater. Sci. Eng. C 117 (2020), 111294.

[28] R.S. Sequeira, S.P. Miguel, C.S. Cabral, A.F. Moreira, P. Ferreira, I.J. Correia, Development of a poly (vinyl alcohol)/lysine electrospun membrane-based drug delivery system for improved skin regeneration, Int. J. Pharm. 570 (2019), 118640.

[29] S.P. Miguel, D. Simões, A.F. Moreira, R.S. Sequeira, I.J. Correia, Production and characterization of electrospun silk fibroin based asymmetric membranes for wound dressing applications, Int. J. Biol. Macromol. 121 (2019) 524–535.

[30] S.P. Miguel, M.P. Ribeiro, H. Brancal, P. Coutinho, I.J. Correia, Thermoresponsive chitosan–agarose hydrogel for skin regeneration, Carbohydr. Polym. 111 (2014) 366–373.

[31] C. Guyot, M. Cerruti, S. Lerouge, Injectable, strong and bioadhesive catechol-chitosan hydrogels physically crosslinked using sodium bicarbonate, Mater. Sci. Eng. C 118 (2021), 111529.

[32] A. Rogina, A. Ressler, I. Matić, G.G. Ferrer, I. Marijanović, M. Ivanković, H. Ivanković, Cellular hydrogels based on pH-responsive chitosan-hydroxyapatite system, Carbohydr. Polym. 166 (2017) 173–182.

[33] M.U.A. Khan, S. Haider, M.A. Raza, S.A. Shah, S.I. Abd Razak, M.R.A. Kadir, F. Subhan, A. Haider, Smart and pH-sensitive rGO/Arabinoxylan/chitosan composite for wound dressing: in-vitro drug delivery, antibacterial activity, and biological activities, Int. J. Biol. Macromol. 192 (2021) 820–831.

[34] I.J. Sabino, R. Lima-Sousa, C.G. Alves, B.L. Melo, A.F. Moreira, I.J. Correia, D. de Melo-Diogo, Injectable in situ forming hydrogels incorporating dual-nanoparticles for chemo-photothermal therapy of breast cancer cells, Int. J. Pharm. 600 (2021), 120510.

[35] R. Khalili, P. Zarrintaj, S.H. Jafari, H. Vahabi, M.R. Saeb, Electroactive poly (p-phenylene sulfide)/r-graphene oxide/chitosan as a novel potential candidate for tissue engineering, Int. J. Biol. Macromol. 154 (2020) 18–24.

[36] K. Kosowska, P. Domalik-Pyzik, M. Sekuła-Stryjewska, S. Noga, J. Jagiełło, M. Baran, L. Lipińska, E. Zuba-Surma, J. Chłopek, Gradient chitosan hydrogels modified with graphene derivatives and hydroxyapatite: physiochemical properties and initial cytocompatibility evaluation, Int. J. Mol. Sci. 21 (14) (2020) 4888.

[37] M. Li, Y. Liang, J. He, H. Zhang, B. Guo, Two-pronged strategy of biomechanically active and biochemically multifunctional hydrogel wound dressing to accelerate wound closure and wound healing, Chem. Mater. 32 (23) (2020) 9937–9953.

[38] K. Ren, Y. Wang, T. Sun, W. Yue, H. Zhang, Electrospun PCL/gelatin composite nanofiber structures for effective guided bone regeneration membranes, Mater. Sci. Eng. C 78 (2017) 324–332.

[39] J. Quirós, S. Gonzalo, B. Jalvo, K. Boltes, J.A. Perdigón-Melón, R. Rosal, Electrospun cellulose acetate composites containing supported metal nanoparticles for antifungal membranes, Sci. Total Environ. 563 (2016) 912–920.

[40] D.R. Figueira, S.P. Miguel, K.D. de Sá, I.J. Correia, Production and characterization of polycaprolactone-hyaluronic acid/chitosan-zein electrospun bilayer nanofibrous membrane for tissue regeneration, Int. J. Biol. Macromol. 93 (2016) 1100–1110.

[41] E. Vatankhah, M.P. Prabhakaran, G. Jin, L.G. Mobarakeh, S. Ramakrishna, Development of nanofibrous cellulose acetate/gelatin skin substitutes for variety wound treatment applications, J. Biomater. Appl. 28 (6) (2014) 909–921.

[42] M. Muralidharan, K. Shinu, A. Seema, Optically triggered actuation in chitosan/reduced graphene oxide nanocomposites, Carbohydr. Polym. 144 (2016) 115–121.

[43] C. Dai, S. Shih, A. Khachemoune, Skin substitutes for acute and chronic wound healing: an updated review, J. Dermatol. Treat. 31 (6) (2020) 639–648.

[44] H.P. Felgueiras, M.T.P. Amorim, Functionalization of electrospun polymeric wound dressings with antimicrobial peptides, Colloids Surf. B: Biointerfaces 156 (2017) 133–148.

[45] P. Feng, Y. Luo, C. Ke, H. Qiu, W. Wang, Y. Zhu, R. Hou, L. Xu, S. Wu, Chitosan-based functional materials for skin wound repair: mechanisms and applications, Front. Bioeng. Biotechnol. 9 (2021), 650598.

[46] S. Dhivya, V.V. Padma, E. Santhini, Wound dressings–a review, Biomedicine 5 (4) (2015) 1–5.

[47] P.I. Morgado, A. Aguiar-Ricardo, I.J. Correia, Asymmetric membranes as ideal wound dressings: an overview on production methods, structure, properties and performance relationship, J. Membr. Sci. 490 (2015) 139–151.

[48] M. Fathi, M. Alami-Milani, M.H. Geranmayeh, J. Barar, H. Erfan-Niya, Y. Omidi, Dual thermo-and pH-sensitive injectable hydrogels of chitosan/(poly (N-isopropylacrylamide-co-itaconic acid)) for doxorubicin delivery in breast cancer, Int. J. Biol. Macromol. 128 (2019) 957–964.

[49] M. Abd El-Hady, S.E.-S. Saeed, Antibacterial properties and pH sensitive swelling of insitu formed silver-curcumin nanocomposite based chitosan hydrogel, Polymers 12 (11) (2020) 2451.

[50] M.A. Wsoo, S.I. Abd Razak, S.P.M. Bohari, S. Shahir, R. Salihu, M.R.A. Kadir, N.H. M. Nayan, Vitamin D3-loaded electrospun cellulose acetate/polycaprolactone nanofibers: characterization, in-vitro drug release and cytotoxicity studies, Int. J. Biol. Macromol. 181 (2021) 82–98.

[51] S. Fahimirad, F. Ajalloueian, Naturally-derived electrospun wound dressings for target delivery of bio-active agents, Int. J. Pharm. 566 (2019) 307–328.
[52] N. Siddiqui, S. Asawa, B. Birru, R. Baadhe, S. Rao, PCL-based composite scaffold matrices for tissue engineering applications, Mol. Biotechnol. 60 (7) (2018) 506–532.
[53] M.N. Nosar, M. Salehi, S. Ghorbani, S.P. Beiranvand, A. Goodarzi, M. Azami, Characterization of wet-electrospun cellulose acetate based 3-dimensional scaffolds for skin tissue engineering applications: influence of cellulose acetate concentration, Cellulose 23 (5) (2016) 3239–3248.
[54] S.P. Miguel, M.P. Ribeiro, P. Coutinho, I.J. Correia, Electrospun polycaprolactone/aloe vera_chitosan nanofibrous asymmetric membranes aimed for wound healing applications, Polymers (Basel) 9 (5) (2017).
[55] S.M. Oliveira, N.M. Alves, J.F. Mano, Cell interactions with superhydrophilic and superhydrophobic surfaces, J. Adhes. Sci. Technol. 28 (8–9) (2014) 843–863.
[56] P. Wu, A.C. Fisher, P.P. Foo, D. Queen, J.D. Gaylor, In vitro assessment of water vapour transmission of synthetic wound dressings, Biomaterials 16 (3) (1995) 171–175.
[57] S.P. Miguel, R.S. Sequeira, A.F. Moreira, C.S.D. Cabral, A.G. Mendonca, P. Ferreira, I.J. Correia, An overview of electrospun membranes loaded with bioactive molecules for improving the wound healing process, Eur. J. Pharm. Biopharm. 139 (2019) 1–22.
[58] M. Ji, J. Li, Y. Wang, F. Li, J. Man, J. Li, C. Zhang, S. Peng, S. Wang, Advances in chitosan-based wound dressings: modifications, fabrications, applications and prospects, Carbohydr. Polym. 297 (2022), 120058.
[59] C. Casadidio, D.V. Peregrina, M.R. Gigliobianco, S. Deng, R. Censi, P. Di Martino, Chitin and chitosans: characteristics, eco-friendly processes, and applications in cosmetic science, Mar. Drugs 17 (6) (2019) 369.
[60] F. Croisier, C. Jérôme, Chitosan-based biomaterials for tissue engineering, Eur. Polym. J. 49 (4) (2013) 780–792.
[61] P. Deng, L. Yao, J. Chen, Z. Tang, J. Zhou, Chitosan-based hydrogels with injectable, self-healing and antibacterial properties for wound healing, Carbohydr. Polym. 276 (2022), 118718.
[62] J. Lu, Y. Chen, M. Ding, X. Fan, J. Hu, Y. Chen, J. Li, Z. Li, W. Liu, A 4arm-PEG macromolecule crosslinked chitosan hydrogels as antibacterial wound dressing, Carbohydr. Polym. 277 (2022), 118871.